RSC Advances

PAPER

View Article Online
View Journal | View Issue

Cite this: *RSC Adv.*, 2025, **15**, 6984

Ultrasonic-assisted europium decorated cuprous oxide nanoparticles: exploring their photothermal capabilities and antioxidant properties for biomedical applications†

Sarmistha Mazumder,[a] Tiasa Das[b] and Raviraj Vankayala *[ab]

Received 20th December 2024
Accepted 25th February 2025

DOI: 10.1039/d4ra08914f

rsc.li/rsc-advances

Metal oxide nanoparticles offer capabilities for cancer therapeutics, but their applicability is often jeopardized due to toxicity hurdles. To tackle this problem, in this study, we have synthesized europium decorated cuprous oxide nanoparticles (Eu–Cu_2O NPs) *via* a facile ultrasonic-assisted method. Surface decoration of nanoparticles is an effective strategy to tailor their physicochemical and biological properties. The decorated nanoparticles were found to possess improved stability, superior biocompatibility and enhanced photothermal properties than the undecorated pristine nanoparticles (Cu_2O NPs). *In vitro* studies validated the capacity of the decorated nanoparticles to regulate the production of reactive oxygen species (ROS) and in turn combat the inherent toxicity of cuprous nanoparticles. By controlling the ROS dynamics and decreasing inadvertent toxic effects minimize possibilities of higher toxicity enabling this innovative strategy to potentially transform into an effective platform for drug delivery systems.

1. Introduction

Combining numerous material characteristics, pertaining to their physicochemical, mechanical and biological properties compared to their bulk forms,[1] nanomaterials have transformed into a prime factor for various healthcare applications. Among the developing engineered nanoparticles, metal-based nanoparticles, including metallic nanoparticles and metal oxide nanoparticles have made an entry into the field of biomedicine. Besides, the widely explored gold, silver, platinum, iron oxide, zinc oxide or titanium dioxide-based nanoparticles, copper-based nanoparticles are gaining traction in environmental and biomedical research, specifically in drug delivery systems and diagnostic or therapeutic interventions.[2–4] Researchers have been motivated to study impact of copper nanoparticle systems on human health as copper is discernibly responsible for a multitude of physiological functions in the body.[5] Owing to their potent properties, cuprous oxide (Cu_2O) nanostructures have been primarily studied as antimicrobial agents for antibacterial, antiviral and antifungal action with few demonstrations of anti-cancer effects.[6,7] These nanoparticles display promising cytotoxic effects, predominantly *via* generation of reactive oxygen species (ROS) leading to the disruption of the redox homeostasis in cancerous cells and ultimately stimulation of cellular death mechanisms.[8–11] However, the bottleneck of this inherent potency stems from the propensity of the Cu_2O nanostructures to overproduce non-specific ROS that raises concerns regarding inadvertent damage to tissues, their physicochemical instability in biological environments lead to aggregation and degradation, further posing challenges for use in clinical settings. Their tendency to exhibit higher toxicity compared to other groups of metal oxide nanoparticles due to spontaneous oxidation, copper ion release,[12–14] or higher ROS generation creates a significant limitation for them to be readily used for an array of biomedical applications, including anti-cancer therapeutics. To harness the therapeutic potential of these nanoparticles while mitigating higher toxic behaviour, researchers are turning to innovative strategies, employing surface decoration or doping techniques to improve the inherent properties of Cu_2O, simultaneously limiting ion release and reducing harmful ROS generation.[15,16]

In the present study, we have synthesised europium-decorated Cu_2O nanoparticles (Eu–Cu_2O NPs) through a facile ultrasonic-assisted method and explored their photothermal, cytotoxic and oxidative properties *in vitro*. Europium, a rare-earth metal primarily used in industrial applications owing to its luminescence property, has recently gained importance for its promising biological functions.[17] Additionally, europium is a popular material for fabricating near infrared (NIR) light-emitting diodes (LEDs) and phosphors for broadband

---

[a] Center for Medical Technologies, Indian Institute of Technology, Jodhpur 342030, Rajasthan, India

[b] Department of Bioscience & Bioengineering, Indian Institute of Technology, Jodhpur 342030, Rajasthan, India. E-mail: rvankayala@iitj.ac.in

† Electronic supplementary information (ESI) available. See DOI: https://doi.org/10.1039/d4ra08914f

emission materials. Nuthalapati *et al.* have shown the use of europium hexaboride (EuB_6) nanoparticles as a nanotheranostic agent in NIR II and III.[18] Hence, investigation of the effect of NIR, influenced by the decoration of europium on Cu_2O NPs, is essential through detailed structural and functional characterisations. Although research groups have explored europium-doped systems as biosensing platforms,[19–21] europium-decorated copper nanosystems specifically, have not been studied for their cytotoxic and oxidative properties, to the best of our knowledge. While Eu–Cu_2O NPs exhibited enhanced photothermal conversion efficiency compared to the undecorated counterparts, they surprisingly demonstrated reduced cellular toxicity and ROS generation in cancer cells. This noteworthy finding of the paradoxical reduction in cytotoxicity of Eu–Cu_2O nanoparticles when compared to the undecorated nanoparticles warrants further investigation. The ability to reduce ROS *via* europium decoration hints at the potential capacity of these nanoparticles to be further explored for combination therapies or as drug delivery systems allowing a controlled delivery due to the biocompatibility imparted by europium. Researchers have demonstrated how europium doped yttrium vanadate nanoparticles reduced the toxicity of cisplatin.[22] In this work, we explored the effects of europium decoration on Cu_2O NPs and the findings suggest that Eu–Cu_2O NPs have great promise in different biomedical applications as the higher toxicity of the Cu_2O NPs can be combatted due to europium surface decoration.

2. Experimental section

2.1 Materials

Copper sulphate ($CuSO_4 \cdot 5H_2O$) and sodium dodecyl sulphate (SDS) were purchased from Himedia Laboratories and Sigma Aldrich, respectively. Europium nitrate ($Eu(NO_3)_3 \cdot 6H_2O$), ascorbic acid and sodium hydroxide were obtained from Sisco Research Laboratories Pvt. Ltd. Murine fibroblast cell line (NIH-3T3) and human epithelial cancer cell line (KB cells) were procured from NCCS, Pune. Dulbecco's Modified Eagle Medium (DMEM), fetal bovine serum (FBS), penicillin–streptomycin and trypsin–EDTA were obtained from Himedia Laboratories. Phosphate buffered saline (PBS) was purchased from Sigma Aldrich.

2.2 Ultrasonic-assisted synthesis of Cu_2O NPs and Eu–Cu_2O NPs

The Cu_2O NPs were synthesised using a modified ultrasonic-assisted solution precursor route method.[23] In a typical experiment, 0.01 M $CuSO_4 \cdot 5H_2O$ and 0.1 M SDS solutions were mixed and subjected to ultrasonic dissolution for 30 min. Subsequently, 0.5 M ascorbic acid and 1.0 M sodium hydroxide (NaOH) were added to the homogeneous copper precursor solution. The resultant solution was allowed to age at room temperature for 24 h, after which it was purified by centrifugation and filtration to obtain the nanoparticles. The obtained Cu_2O NPs were dried and used for further characterisation. To obtain the europium decorated cuprous oxide nanoparticles (Eu–Cu_2O NPs), the copper precursor solution was ultrasonically prepared using the same method as mentioned above. Aqueous solution of $Eu(NO_3)_3 \cdot 6H_2O$ was added to the solution of $CuSO_4 \cdot 5H_2O$ and SDS at varying weights (0.1%, 0.25% and 0.5%). The solution was further ultrasonically treated for another 30 min. A similar incubation period of 24 h after adding ascorbic acid and NaOH was employed. Eu–Cu_2O NPs were ultimately obtained using similar purification techniques and subjected to further characterisation (Scheme 1).

2.3 Characterization of Cu_2O NPs and Eu–Cu_2O NPs

The as-synthesised nanoparticles were extensively characterised and investigated to explore their physicochemical and optical properties through various analytical techniques. The morphologies and particle sizes were inspected using a Field Emission Scanning Electron Microscope (Thermo Scientific Apreo 2 FESEM). The hydrodynamic sizes, polydispersity index (PDI) and zeta potential of the nanoparticles were confirmed with the help of Dynamic Light Scattering (Analytical Zetasizer Ultra, Malvern). To verify the crystallographic structures or alterations of the undecorated and decorated Cu_2O nanoparticles, X-ray Diffraction (XRD) patterns were recorded at room temperature on a Powder X-ray Diffractometer (D8 Advance, Bruker) with a Cu K-alpha source ($\lambda = 1.5418$ Å). The crystallite size was further analysed from the XRD data using the Scherrer equation, given by:

$$D = (K\lambda)/(\beta \cos \theta) \qquad (1)$$

where D: crystallite size (nm), K: shape factor (0.9 for spherical nanoparticles), λ: for Cu K-alpha, 0.15418 nm, β: Full Width at Half Maximum (FWHM) of the peak (in radians), and θ: Bragg angle (in radians). To study the chemical state and composition of both the nanoparticles and to confirm the decoration of europium, X-ray Photoelectron Spectroscopy (XPS, Thermo Scientific NEXA Surface analyser) and Fourier Transform Infrared (FTIR) spectroscopy (Thermo Scientific Nicolet iS10) were utilised. The optical properties were determined by analysing the absorption and fluorescence spectra using the UV-visible/NIR spectrophotometer (Jasco 7300) and spectrofluorometer (Jasco-FP 8300), respectively.

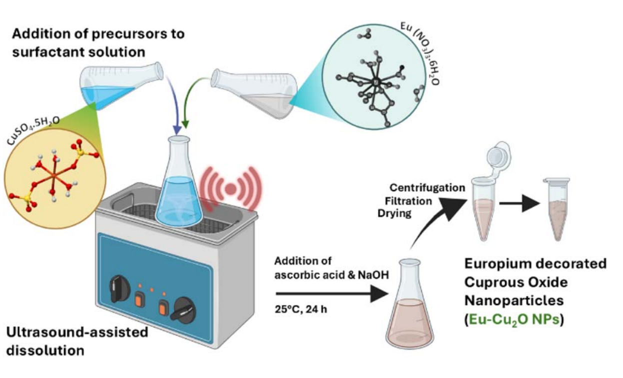

Scheme 1 Schematic for the ultrasonic-assisted synthesis of europium decorated cuprous oxide nanoparticles (Eu–Cu_2O NPs).

2.4 Investigation of photothermal properties of Cu_2O NPs and Eu–Cu_2O NPs

The aqueous suspensions (1 mg mL^{-1}) of the Cu_2O NPs and Eu–Cu_2O NPs were irradiated using an 808 nm NIR laser at a power density of 1 W cm^{-2} for specific time durations. The photothermal conversion efficiencies were also calculated for both the types of nanoparticles and the details were provided in the ESI.†

2.5 Quantification of cellular viabilities using MTT assay

To evaluate the cytotoxicity effects of both Cu_2O NPs and Eu–Cu_2O NPs, NIH-3T3 and KB cells were seeded at a density of 1.0×10^4 cells per well in 96-well plates and allowed to adhere to the surface for 24 h. The following day, various concentrations of Cu_2O NPs and Eu–Cu_2O NPs were added to the respective wells and further incubated in the dark at 37 °C for 24 h. Post incubation with nanoparticles, the media was discarded, and excess nanoparticles were washed off with the help of phosphate-buffered saline (PBS). Subsequently, MTT (0.5 mg mL^{-1}) with media was added to the cells to measure cellular viability. After 2 h of incubation, the media with MTT was carefully aspirated, and 1 mL of dimethyl sulfoxide (DMSO) was added to dissolve the formazan crystals. The optical absorbance values at 570 nm were recorded using a multimode microplate reader (BioTek, Agilent). The untreated cells were taken as the controls for the MTT experiments.

2.6 *In vitro* cellular death assessment using flow cytometry

KB cells were seeded in 12-well plates at a density of 1.0×10^5 cells per well and incubated for 24 h. Post incubation, 10 and 50 μg mL^{-1} of Cu_2O NPs and Eu–Cu_2O NPs were added to the specific treatment wells under the dark and light irradiation conditions, followed by further incubation for 4 h. Following treatment, the specific treated groups were irradiated with an 808 nm NIR laser at a power density of 1 W cm^{-2} for 10 min under identical conditions. The trypsinized cells were resuspended in 500 μL of 1× PBS, followed by the addition of propidium iodide (1.5 μM) and incubation for 30 min at room temperature in the dark. Thereafter, the samples were recorded for cellular death analysis using flow cytometry (BD FACSDiscover S8). Untreated and ethanol-treated cells were used as negative and positive controls for the experiment.

2.7 *In vitro* ROS generation using flow cytometry

The intracellular ROS generation was investigated using the 2,7-dichlorofluorescein diacetate (DCFH-DA) fluorescent probe. Briefly, KB cells were seeded in 12-well plates at a cellular density of 1.0×10^5 cells per well and allowed to adhere for 24 h. The next day, the cells were pretreated with 10 μM DCFH-DA and incubated for 30–45 min at 37 °C in the dark. The treated cells with 10 μg mL^{-1} and 50 μg mL^{-1} of Eu–Cu_2O NPs and Cu_2O NPs were allowed to interact with nanoparticles for 4 h for both the dark and light experiments. Following treatment, the specific treated groups were photo-irradiated with 808 nm NIR laser at a power density of 1 W cm^{-2} for 10 min under identical conditions. The trypsinized cells for both dark and light-irradiated groups were investigated for the DCFH-DA fluorescence through the FITC channel in the flow cytometer. Untreated cells were used as the control for this experiment. To identify the species of ROS generated, the cells were pretreated with DCFH-DA, followed by incubation with the Eu–Cu_2O NPs for 4 h. ROS quenchers, D-mannitol (10 mM) and L-histidine (50 mM) were added for 60 min prior to completion of nanoparticle incubation. The mean fluorescence intensities of the DCFH-DA in presence and absence of ROS quenchers were estimated using the similar flow cytometric method.

3. Results and discussion

3.1 Physicochemical properties of Cu_2O NPs and Eu–Cu_2O NPs

The Cu_2O NPs and Eu–Cu_2O NPs were synthesised using a simple and green ultrasonic-assisted synthesis approach. We have used variable concentrations of europium ions to decorate on the surface of Cu_2O NPs. As measured using dynamic light scattering (DLS), the pristine Cu_2O NPs were found to have a hydrodynamic mean diameter of 236.67 ± 1.52 nm with a polydispersity index (PDI) of 0.13 and a surface charge of −22.1 ± 0.12 mV (see Fig. S1 and Table S1†). The decorated Cu_2O NPs with various amounts of europium ions were also investigated for their average particle size, PDI and zeta potential. A significant change in terms of zeta potential was noted for the group decorated with 0.25 wt% of europium. The Eu–Cu_2O NPs (0.25 wt%) had an increase in the surface charge, measured at 17.8 ± 0.38 mV, which suggests successful decoration of europium ions when compared to the undecorated and other decorated Cu_2O NPs. The hydrodynamic mean diameter for Eu–Cu_2O NPs (0.25 wt%) is 229.33 ± 17.89 nm, respectively. Considering the hydrodynamic mean diameters, PDI and zeta potential values of all the sample groups, Eu–Cu_2O NPs (0.25 wt%) was found to be optimal for further studies. The morphological analysis of Cu_2O NPs and Eu–Cu_2O NPs were performed using field emission scanning electron microscopy (FESEM). As shown in Fig. 1a and b, both the Cu_2O NPs and Eu–Cu_2O NPs were found to be spherical in shape. However, considerable aggregation was seen in Cu_2O NPs. The reduced aggregation in the case of Eu–Cu_2O NPs could result from the enhanced electrostatic repulsion between the nanoparticles in suspension due to a higher positive surface charge following decoration with positively charged europium ions. The Cu_2O NPs were observed to have smooth surfaces. However, the Eu–Cu_2O NPs were noted to have slightly uneven surfaces, suggesting surface attachment. The TEM images in Fig. S2† also confirmed the particle morphologies as depicted by FESEM. Analysing the size distribution of the as synthesised nanoparticles (Fig. 1c and d), it was found that Cu_2O NPs with a mean hydrodynamic diameter of 236.67 ± 1.52 nm had a less broad size distribution than the Eu–Cu_2O NPs with 229.33 ± 17.89 nm. The variable sizes indicate a cumulative effect of the sonication cycles and the decoration process.

Further, X-ray diffraction data for the as synthesized Cu_2O NPs and Eu–Cu_2O NPs reveals that they are crystalline in nature,

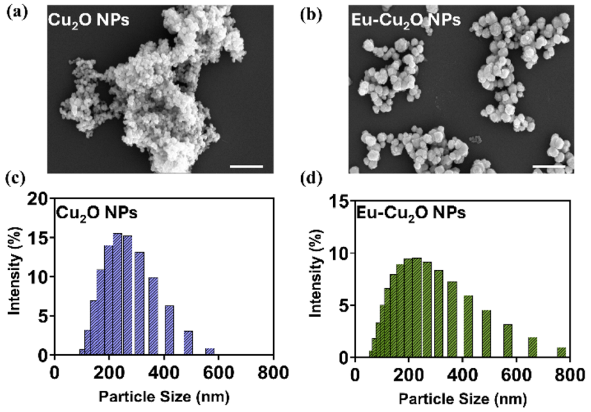

Fig. 1 FESEM images of (a) Cu_2O NPs (b) Eu–Cu_2O NPs. The scale bar is 1 μm, DLS size distribution of (c) Cu_2O NPs (d) Eu–Cu_2O NPs.

and the diffraction peaks match with the reference Cu_2O (JCPDS card no. 98-009-6117) (see Fig. 2a). The X-ray diffraction peaks with (111) lattice plane for both the Cu_2O NPs and Eu–Cu_2O NPs were shown and Rietveld refinement was applied to calculate the lattice parameters. The pristine Cu_2O NPs showed distinct peaks designated as (110), (111), (200), (220) and (311) at 2θ values of 29.5°, 36.4°, 42.3°, 61.3° and 73.5° respectively, corresponding to a cubic crystal structure. No additional peaks or amorphous content was detected, hence confirming the phase purity of the synthesised Cu_2O NPs. Further, to detect the effects of decoration of europium ions, the crystalline structure of Eu–Cu_2O NPs was analysed similarly. It was interesting to note that the significant peaks in Eu–Cu_2O NPs mirrored those found for pristine Cu_2O NPs, indicating no incorporation of europium into the crystal lattice of the Cu_2O NPs, instead, a surface decoration was obtained as desired. However, the (111) diffraction peak at 36.4° was magnified to observe minimal peak shift but a broadening for Eu–Cu_2O NPs as compared to Cu_2O NPs, suggesting a defect or reduction in crystallite size due to the introduction of a foreign material.[21] The peak shifts usually indicate the lattice strain or interaction between the central matrix and the decorative species. In this case, the minimal shift stipulated that the europium ions were surface decorated without interfering with the crystal structure of Cu_2O. Following the analysis (see the details in ESI†), the crystallite size was found to be 21.37 nm and 14.28 nm for Cu_2O NPs and Eu–Cu_2O NPs, respectively. The FTIR analysis was used to study the surface functionalities and the vibrational modes of the undecorated Cu_2O NPs and Eu–Cu_2O NPs. The characteristic peak at 629 cm^{-1} for pristine Cu_2O NPs indicates Cu–O stretching vibrations. The minimal shift for this peak to 627 cm^{-1} in Eu–Cu_2O NPs verifies that the Cu_2O structure is preserved, and slight surface modifications are present due to europium decoration. Following the decoration of europium, the observed shifts from 3487 cm^{-1} to 3470 cm^{-1} and 1631 cm^{-1} to 1618 cm^{-1} advocate a possible interaction of europium with surface hydroxyl groups or adsorbed water molecules dictating the O–H stretching and bending vibrations. Shifts from 1400 cm^{-1} to 1366 cm^{-1}, 1184 cm^{-1} to 1193 cm^{-1} and 1106 cm^{-1} to 1117 cm^{-1} could be stemming from the minor changes in the chemical environment under the influence of europium. The appearance of a new peak at 990 cm^{-1} in the Eu–Cu_2O spectrum could arise from Eu–O bonds validating its integration on the surface. Specifically, the 990 cm^{-1} FTIR peak in Eu–Cu_2O NPs is likely associated with specific vibrational modes related to the Eu^{3+} ions and their interaction with the Cu_2O (copper(I) oxide) surface through Eu–O or Eu–Cu–O bonds. Overall, the 990 cm^{-1} peak in Eu–Cu_2O NPs is likely due to a vibrational mode associated with the interaction between Eu^{3+} ions and Cu_2O, possibly Eu–O bond stretching or surface-related species like hydroxyl groups or ligands. The peak is not a typical Cu–O vibration but could be related to the coordination chemistry of europium or specific surface interactions (see Fig. 2b).

X-ray photoelectron spectroscopy (XPS) was utilised to evaluate the chemical composition and electronic structure of Eu–Cu_2O NPs. The XPS survey spectrum of Eu–Cu_2O NPs in revealed the presence of europium, copper and oxygen species (see Fig. 3a). The presence of carbon is due to the reaction component, ascorbic acid. The high resolution XPS spectrum of Eu 3d for Eu–Cu_2O NPs showed a characteristic binding energy peak centered at 1135 eV, which confirmed the surface decoration of europium ions on the surface of Cu_2O NPs (Fig. 3b).[24] The high resolution XPS spectra for Cu 2p, O 1s and C 1s also

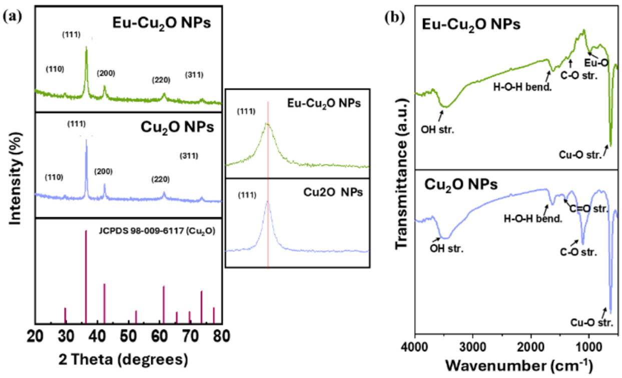

Fig. 2 (a) XRD spectra of Eu–Cu_2O NPs and Cu_2O NPs with magnified (111) peak, (b) FTIR spectra of Eu–Cu_2O NPs and Cu_2O NPs.

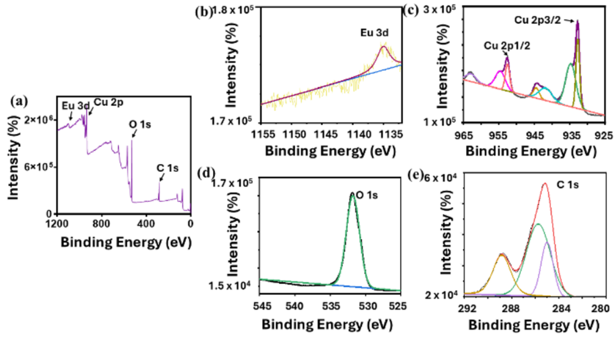

Fig. 3 (a) XPS survey spectrum of Eu–Cu_2O NPs, elemental XPS spectra for (b) Eu 3d (c) Cu 2p (d) O 1s and (e) C 1s.

corroborated their presence, indicating the specific peaks with their corresponding binding energies. Specifically, the XPS peaks at 932.7 eV and 952.6 eV, indicated as the Cu $2p_{3/2}$ and $2p_{1/2}$ electronic states of copper, respectively. The satellite peaks at 941 eV and 944.1 eV confirms the presence of Cu(I) and complex electronic interactions in Eu–Cu_2O NPs (Fig. 3c). The additional peak observed at 962.9 eV could result from secondary effects or the presence of other components and is not characteristic of copper.[25] The O 1s spectrum with the characteristic binding energy peak at 531.7 eV indicate the presence of oxygen with transitional forms such as hydroxyl groups or moisture-related species.[26] The C 1s spectrum showed the characteristic binding energy peaks centered at 285 and 288 eV (see Fig. 3d and e). The Cu 2p elemental spectrum of pristine Cu_2O NPs (Fig. S3†) showed the characteristic peaks at 932.6 and 952.6 eV for $2p_{3/2}$ and $2p_{1/2}$ electronic states, respectively. The absence of satellite peaks corroborates a more localised and less dispersive electronic distribution in pristine Cu_2O NPs, favouring lesser excitations for shake-up transitions.[26]

The extensive physicochemical characterisation of Cu_2O NPs and Eu–Cu_2O NPs through various analytical techniques cumulatively demonstrated the successful decoration of europium ions on the surface of pristine Cu_2O NPs to obtain Eu–Cu_2O NPs.

3.2 Optical properties of Cu_2O NPs and Eu–Cu_2O NPs

Both copper and europium are significantly potent optical materials. However, the impact of europium decoration on the optical properties of Cu_2O NPs were not explored yet. The absorption spectrum of pristine Cu_2O NPs showed absorbance in the UV-visible range, with a peak at 482 nm, including broad peaks around the region of 260 nm and 380 nm, due to electronic transitions from the valence band to the conduction band (see Fig. 4a, inset: digital images of both nanoparticle solutions under ambient conditions). The ability of the Cu_2O NPs to absorb light in the near-infrared (NIR) region was also noted. However, no significant peaks were observed in the NIR region. In contrast, distinct absorption peaks were found for Eu–Cu_2O NPs at 294 nm, 364 nm and 460 nm with a tail extending in the NIR region. The peak at 460 nm could be attributed to the transition between $^7F_0$ to $^5D_2$ under the specific influence of europium decoration on Cu_2O NPs, as this significantly marks the presence of Eu^{3+} ions.[27,28] The direct band gap energy for the synthesised Cu_2O NPs was calculated using a Tauc plot analysis (Fig. S4†) using the absorption spectrum, and was found to be ~2.56 eV. The optical band gap of Cu_2O has been reported to be between 2.23 eV to 2.56 eV in the previous studies.[29] Due to the favourable direct bandgap transitions, Cu_2O NPs have been extensively explored in semiconductors, photovoltaics, photocatalysis, sensors, phototherapy, *etc.* The direct band gap energy for the Eu–Cu_2O was also calculated similarly to inspect the impact of decoration. The value was found to be 2.71 eV, which denoted a wide band gap for both Eu–Cu_2O NPs and Cu_2O NPs. The respective band gaps were found to be inversely related to the estimated crystallite sizes of Cu_2O NPs and Eu–Cu_2O NPs. The decoration with europium demonstrated quantum confinement and allowed surface interactions that altered band gap depending on the material properties and nature of interaction.[30] The fluorescence property was also analysed by measuring the fluorescence intensities of the Cu_2O NPs and Eu–Cu_2O NPs. Europium is a well-known luminescent material that shows typical fluorescence peak characteristics. As shown in the inset of Fig. 3b, the precursor, europium hexanitrate, when excited at 390 nm, showed emission peaks centered at 558 nm, 588 nm, 616 nm and 694 nm corresponding to the electronic transitions from $^5D_1$ to $^7F_2$, $^5D_0$ to $^7F_1$, $^5D_0$ to $^7F_2$ and $^5D_0$ to $^7F_4$ respectively.[31]

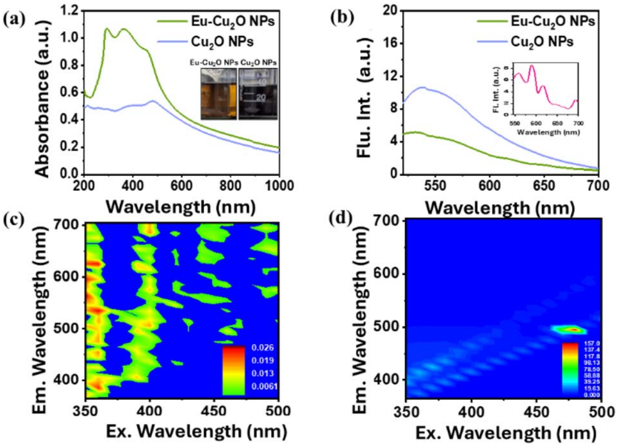

Fig. 4 (a) Absorbance spectra of Eu–Cu_2O NPs and Cu_2O NPs, (b) fluorescence emission spectra of Eu–Cu_2O NPs and Cu_2O NPs (inset: emission spectra of europium nitrate), excitation–emission mapping of (c) Eu–Cu_2O NPs and (d) Cu_2O NPs.

However, there is no noticeable fluorescence signal observed from Cu_2O NPs or Eu–Cu_2O NPs when excited at 390 nm. This could be presumably due to the quenching effect of copper on europium ions, which was inferred from the fluorescence analysis and excitation-emission mapping that might have resulted from electron transfer or energy transfer processes (Fig. 4b–d). Szyszka *et al.* observed that in presence of copper ions, emission quenching of europium is a dominant phenomenon and proposed a quenching mechanism. The efficiency of quenching was directly proportional to the concentration of europium.[32] The emission quenching of europium ions was attributed to nonradiative energy transfer between Eu^{3+} and Cu^{2+} ions, which was facilitated by electric dipole interaction.[33,34] Overall, the decorated Eu–Cu_2O NPs could have limited potential for imaging applications, despite utilising two luminescent materials.

3.3 Photothermal properties of Cu_2O NPs and Eu–Cu_2O NPs

The NIR absorption for both the nanoparticles has led to a hypothesis that Cu_2O NPs and Eu–Cu_2O NPs might show promising photothermal properties. To investigate the photothermal properties, Cu_2O NPs and Eu–Cu_2O NPs were exposed to 808 nm NIR light irradiation at a power density of 1 W cm^{-2} for 15 min to monitor the temperature rise. As shown in Fig. 5a, NIR-induced temperature change (ΔT) in Eu–Cu_2O NPs was ~20 °C as opposed to 6 °C in Cu_2O NPs. This significant finding suggested that the Eu–Cu_2O NPs could be a suitable candidate for applications involving light-to-heat conversion. Further, to study the stability of these nanoparticles on 808 nm NIR light irradiation, four on-and-off cycles were considered, which showed a noticeable decrement in the photostability of Cu_2O NPs as compared to Eu–Cu_2O NPs (Fig. 5b). These findings validated the ability of the nanoparticles to absorb light and convert the absorbed photons into heat. The photothermal conversion efficiency (η)[35] was calculated using the photothermal effect of one on–off cycle and the linear time data obtained from the cooling period (Fig. 5c–f). It was found to be 44% and 36% for Eu–Cu_2O NPs and Cu_2O NPs, respectively. The details of the η% have been provided in the ESI.† Estimating the η% enables the potential of these nanoparticles for use in phototherapeutic applications.

3.4 Cytotoxic behaviour of Cu_2O NPs and Eu–Cu_2O NPs *in vitro* using MTT assay

One of the most predominant issues with nanomaterials is their toxicity concerns. Studies have shown that while bulk materials do not exhibit measurable toxic effects, nanomaterials often show strong cytotoxic effects in a cell-line-specific and concentration-dependent manner.[36] Studies have demonstrated copper nanoparticles to possess varying degrees of cytotoxicity based on cell lines.[7,37,38]

Hence it is imperative to analyse the interaction between the cells and the synthesised undecorated Cu_2O NPs and europium-decorated Eu–Cu_2O NPs. As shown in Fig. 6a, NIH-3T3, a murine fibroblast cell line, was treated with several concentrations of both nanoparticles and tested for cellular viability using the MTT assay.[39] The lowest concentration of 5 μg mL^{-1} did not show any significant effects between the two nanoparticles. However, with increased concentration, the Cu_2O NPs exhibited more potent cytotoxic effects on the healthy cell line than Eu–Cu_2O NPs. At concentrations of 50 μg mL^{-1} and 100 μg mL^{-1}, Eu–Cu_2O NPs displayed cellular viability of around 86% and 81%, whereas Cu_2O NPs caused a reduction in cellular viability measured around 41% and 38%, respectively. Cumulatively, Cu_2O NPs showed predominant cytotoxic effects on the NIH-3T3 cell line at the mentioned higher concentrations. Previous reports suggest that copper nanoparticles below 25 μg mL^{-1} exhibit minimal toxicity in various normal cell lines, while higher concentrations tend to progressive cytotoxicity.[40] The Eu–Cu_2O NPs were found to be biocompatible at the specific concentrations for the healthy cell line. Eu–Cu_2O NPs and Cu_2O NPs were also tested for their cytotoxic behaviour in the epithelial cancer cell line, KB (Fig. 6b). Herein, 50 μg mL^{-1} elicited a significant difference in the effects of the two nanoparticles on the cellular viability of the cancer cells. Eu–Cu_2O NPs and Cu_2O NPs displayed 64% and 50% cellular viability, respectively. However, the other concentrations did not show any significant variation between the two samples, though both nanoparticles showed more than 50% cellular death at the highest concentration, *i.e.* 100 μg mL^{-1}. The cellular viability experiments were done in the dark using the MTT assay, and the findings corroborated the strong cytotoxic nature of Cu_2O NPs. The Eu–Cu_2O NPs were found to be biocompatible for the healthy cell line, whereas induced comparative greater cellular death in the cancerous cell line.

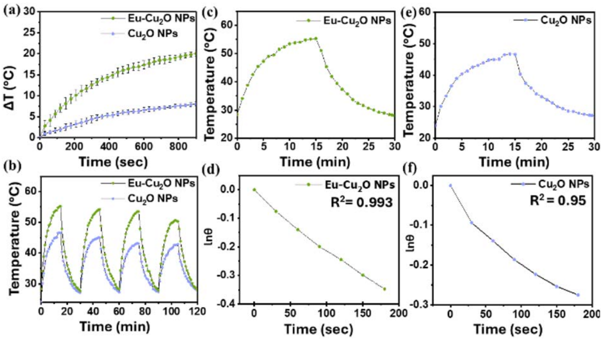

Fig. 5 (a) Photothermal temperature rise for Eu–Cu_2O NPs and Cu_2O NPs using 808 nm laser at 1 W cm^{-2}. Mean values and error bars calculated, $n = 3$, (b) photostability for Eu–Cu_2O NPs and Cu_2O NPs for four ON–OFF cycles with 808 nm laser. (c) Photothermal effect of the irradiation of the aqueous solution of the Eu–Cu_2O NPs with the 808 nm laser (15 min; 1 W cm^{-2}). The laser was turned off after 15 min post irradiation. (d) Linear time data *versus* ln(θ) obtained from the cooling period of (c), (e) photothermal effect of the irradiation of the aqueous solution of the Cu_2O NPs with the 808 nm laser (15 min; 1 W cm^{-2}). The laser was turned off after 15 min post irradiation. (f) Linear time data *versus* ln(θ) obtained from the cooling period of (e).

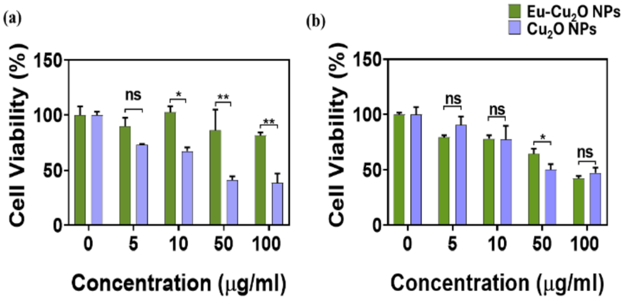

Fig. 6 Cellular viability assay using MTT (dark) of Eu–Cu_2O NPs and Cu_2O NPs treated (a) NIH-3T3 (b) KB cell line. Bars represent the mean of three replicate experiments with standard deviation. The statistically significant differences are indicated as $^*p < 0.05$, $^{**}p < 0.0001$, as calculated using the two-way ANOVA test.

3.5 NIR-activated cytotoxic behaviour of Cu_2O NPs and Eu–Cu_2O NPs *in vitro* using propidium iodide (PI) cell death assay

The undecorated pristine Cu_2O NPs and decorated Eu–Cu_2O NPs did not exhibit a comparative predominant effect on the cancer cell line KB in the dark. To assess the suitability for possible phototherapeutic applications, monitoring the cytotoxic behaviour of both the nanoparticles in dark and light-irradiated conditions is vital. The fluorescent dye PI was used as an indicator for cell death as it binds to the DNA in dead or dying cells and cannot pass through the intact plasma membrane of living cells.[41] The fluorescent signal was captured on a flow cytometer to differentiate between the live cells and those that have uptaken PI. The experiments were conducted in dark and light-irradiated conditions using the previously mentioned parameters to evaluate the NIR light-induced cytotoxic behaviour of the Cu_2O NPs and Eu–Cu_2O NPs. Fig. S5a and b† showed the negative and positive populations in terms of PI fluorescence using a dot plot analysis. A total count of 20 000 cells was taken for the flow cytometric analysis. The KB cells were treated with 10 μg mL^{-1} and 50 μg mL^{-1} of Eu–Cu_2O NPs and Cu_2O NPs and assessed for cellular death in the dark. Fig. S5c and d† exhibited the concentration-dependent significantly higher toxicity of Cu_2O NPs. In comparison, Eu–Cu_2O NPs (Fig. S5e and f†) displayed a much-reduced cellular death pattern. Fig. 7a represents the histogram displaying the PI fluorescence for the whole cell population of all the samples, where increased fluorescence signal intensities were noted in case of Cu_2O NPs treated cells depicting higher numbers of compromised or dead cells, particularly at the concentration of 50 μg mL^{-1}.

To investigate the NIR-responsive cytotoxic behaviour of Cu_2O NPs and Eu–Cu_2O NPs, the treated KB cells were irradiated with an 808 nm NIR laser and analysed for PI fluorescence. Fig. S6a and b† depict the negative (untreated) and positive (death-induced) cell populations used for the analysis. Cu_2O NPs presented with more cellular death, as compared to the Eu–Cu_2O NPs (Fig. S6c–f†). Fig. 7b represents the histogram displaying the PI fluorescence for the whole cell population of all the light irradiated samples, where increased fluorescence signal intensities were noted in case of Cu_2O NPs treated cells depicting higher numbers of compromised or dead cells, as compared to the Eu–Cu_2O NPs treated cells. Cu_2O NPs or Eu–Cu_2O NPs did not exhibit statistically significant NIR activatable cellular behaviour at the specific concentration studies for the KB cell line. Although, under both dark and irradiated conditions, the decoration of europium on Cu_2O NPs predominantly minimised the cytotoxicity caused by the undecorated Cu_2O NPs (Fig. 7c). The mean fluorescence intensities of the treatment groups were calculated and plotted to observe the relationship between Eu–Cu_2O NPs and Cu_2O NPs causing cellular death in the dark and under the influence of NIR irradiation.

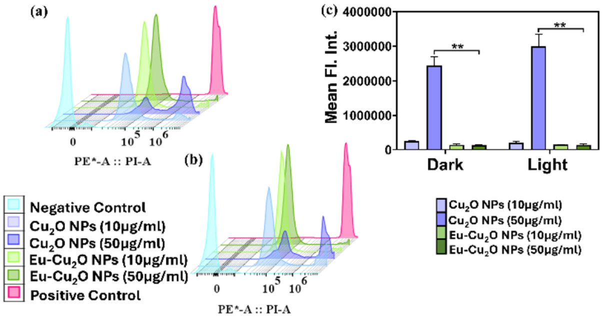

Fig. 7 (a) Flow cytometric staggered histograms of all samples in dark, (b) flow cytometric staggered histograms of all samples under NIR irradiation, (c) bars represent the median MFI (mean fluorescence intensity) of all the samples in dark and light irradiated conditions in two replicates with standard deviation as error bars. The statistically significant differences in between Cu_2O NPs and Eu–Cu_2O NPs at 50 μg mL^{-1} are indicated as $^{**}p < 0.0001$, as calculated using the two-way ANOVA test.

The present analysis was executed considering specific concentrations of both the nanoparticles which established that the europium decorated nanoparticles potentially reduced cytotoxicity, strengthening the findings in previous studies.[42] However, the confirmation of a threshold concentration would require further exploration of the concentration dependent cytotoxic activities in various cell lines. Through our studies, we investigated the NIR responsiveness of Cu_2O NPs and Eu–Cu_2O NPs. Though Eu–Cu_2O NPs displayed enhanced photothermal response, the same property could not be adequately utilised to elicit photothermal death in *in vitro* cancer model. In contrast, we observed an ameliorating effect of europium on the inadvertent toxicity of Cu_2O NPs. Hence, the potential of Eu–Cu_2O NPs as NIR mediated agents for different biomedical applications can be considered promising and deserves extensive research.

3.6 ROS generation by Cu_2O NPs and Eu–Cu_2O NPs *in vitro* using DCFH-DA assay under the influence of NIR irradiation

The higher cytotoxic behaviour of the Cu_2O NPs could presumably be due to the increased tendency of generation of ROS. Copper nanoparticles have been widely studied in relation to the production of ROS.[43] Through our study, it was noted that the Eu–Cu_2O NPs displayed antioxidative characteristics by limiting the ROS production. Europium has been found to impart antioxidant properties to other materials.[44–47] To validate ROS generation as a possible mechanism of the cellular death observed in the previous experiments, DCFHDA assay was employed, and the quantitative fluorescence was calculated through flow cytometry to estimate the production of total ROS.[48]

As seen in Fig. S7b and c,† the Cu_2O NPs caused evident total ROS increase than untreated (Fig. S7a†), in both concentrations at 10 μg mL^{-1} and 50 μg mL^{-1}. However, there was a considerable decrease in ROS production by Eu–Cu_2O NPs (Fig. S7d and e†). The cumulative ROS generation patterns among the two nanoparticles support the cellular death observed previously in KB cells and simultaneously suggest that europium decoration on the Cu_2O NPs has a limiting effect on the detrimental attributes of Cu_2O NPs, which could potentially be leveraged as a protective mechanism for multiple biological applications. Fig. 8a portrays the staggered histogram displaying the green fluorescence of DCFH-DA in the FITC channel for the whole cell population of all the treated samples, where increased fluorescence signal intensities were noted in case of Cu_2O NPs treated cells depicting higher ROS generation, as compared to the Eu–Cu_2O NPs treated cells. It was also seen, that in the presence of NIR irradiation, the europium decoration effectively limited cytotoxicity of the Cu_2O NPs. Hence, ROS production was also investigated under NIR irradiation. A reduction in ROS levels generated was observed that further connoted europium decorated Eu–Cu_2O NPs have a significant effect on the decreased cytotoxicity of Cu_2O NPs through mediation of ROS production.

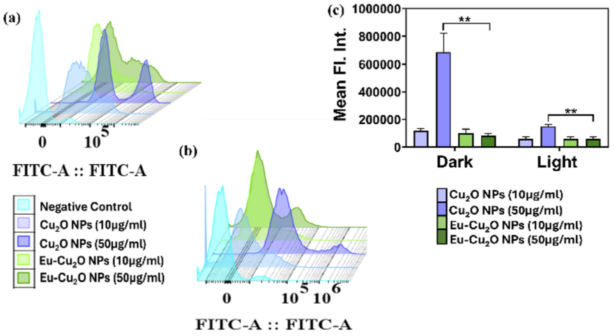

Fig. 8 (a) Flow cytometric staggered histograms of all treated samples indicating fluorescence signals due to DCFH-DA, (b) flow cytometric staggered histograms of all light irradiated samples, (c) bars represent the median MFI (mean fluorescence intensity) of all the samples in dark and light irradiated conditions in two replicates with standard deviation as error bars. The statistically significant differences in between Cu_2O NPs and Eu–Cu_2O NPs at 50 µg mL^{-1} are indicated as $**p < 0.05$, as calculated using the two-way ANOVA test.

As observed in Fig. S8b–e,† the Eu–Cu_2O NPs displayed a notably diminished role in producing ROS than the Cu_2O NPs. Fig. 8b shows the histogram for the DCFHDA fluorescence intensities in the treated samples. The mean fluorescence intensities of the treatment groups were measured and plotted (Fig. 8c) to observe the ROS generation tendencies in between Cu_2O NPs and Eu–Cu_2O NPs in both dark and light conditions. It was similarly noticed that Eu–Cu_2O NPs played a crucial role in combatting the harmful effects of Cu_2O NPs through its antioxidant effects.

However, NIR irradiation was not found to significantly affect the enhancement of the protective antioxidant function of the Eu–Cu_2O NPs at the taken concentrations. Representative images of cells showing DCFH-DA fluorescence have been provided in ESI (Fig. S9†). Cumulatively, the Eu–Cu_2O NPs and Cu_2O NPs displayed synchronous cytotoxic and ROS generation capabilities, however the ameliorating effect of the europium decoration was predominantly noted. Furthermore, to understand the existence of specific ROS, we hypothesized that hydroxyl radicals and singlet oxygen may be the primary reactive oxygen species (ROS) generated by the photoexcitation of Eu–Cu_2O NPs, based on the mechanism of its action and similar studies.[49–51] While the ROS quenching studies did not show statistically significant changes in mean fluorescent intensities of the individual groups, we observed a trend towards decreased intensity with L-histidine, suggesting a potential role of singlet oxygen. The lack of statistical significance could be due to the relatively low ROS concentrations generated as we found in our study that europium decoration has led to reduction in ROS generation as compared to the pristine Cu_2O NPs (Fig. S10†).

In general, it must be noted that surface decoration attributes of the europium decorated Cu_2O NPs (Eu–Cu_2O NPs) can be better revealed with the precise structural characterization and this in turn dictates their behaviour in the biological environment and the cytotoxic action ultimately. In the process, the stability and therapeutic effect can be tailored while potentially reducing inadvertent cytotoxic effects of the nanoparticles. The introduction of europium offers multiple advantages; (i) enhanced stability (ii) controlled oxidative and cytotoxic response (iii) improved biocompatibility. The preliminary findings in our study corroborates that europium decoration is a promising strategy to cater to the higher toxicity concerns of metal oxide nanoparticles.

4. Conclusions

In summary, we have reported the facile ultrasonic-assisted synthesis of europium decorated Cu_2O NPs and studied the effect of europium decoration on the physical, optical and biological properties of Cu_2O NPs. Furthermore, the finding that the addition of europium to Cu_2O nanoparticles lowered the toxicity and ROS production offers a fascinating and potentially significant leap forward in the building of safer and more efficient nanomaterials for use in biomedical applications. The electron scavenging capabilities of europium, its possible impact on copper ion release, and its capacity to regulate cellular uptake are some of the possible causes of this reduction in toxicity. Europium's function in improving biocompatibility and encouraging biodegradability may also help to lessen these nanoparticles' long-term toxicity. Additionally, Eu–Cu_2O NPs decreased toxicity may provide a foundation for the utilisation of these nanoparticles for drug delivery applications. However, more study is necessary to clarify the underlying mechanisms and to fully realize the promise of Eu–Cu_2O NPs. It might be able to achieve the perfect balance between therapeutic efficacy and low side effects by optimizing the characteristics of these nanoparticles, opening the door to more focused and efficient therapeutics. The nanoparticles were found to demonstrate promising capability in modulating the cytotoxicity conventionally associated with pristine Cu_2O NPs, through regulating the ROS production, presumably limiting copper ion release, which are contributors to cytotoxicity. Despite these improvements, statistically significant NIR dependent photothermal cell death was not observed in KB cells. Structural and functional characterization of the Eu–Cu_2O NPs validated the efficacy of europium decoration in enhancing the stability and biocompatibility of Cu_2O NPs, providing a promising avenue for their favourable integration into biomedical applications. The findings underscore the role of europium as an effective surface modifier, suggesting that further exploration of rare-earth element decorations may yield additional improvements in the functional and biocompatibility profiles of metal oxide nanoparticles. This work establishes a foundation for developing safer, more effective Cu_2O-based nanomaterials, supporting their potential use in therapeutic and diagnostic applications where controlled cytotoxicity is essential. Though our system, with unique photothermal properties, did not elicit adequate capabilities as a phototherapeutic agent at the experimental conditions explored, but the effects of europium on the pristine Cu_2O NPs pave the way for inspecting these nano systems for a plethora of other biomedical applications including drug delivery systems, diagnostic imaging, biosensors, *etc.*

Data availability

The data supporting this article have been included as part of the ESI.†

Author contributions

S. M.: conceptualization, methodology, investigation, formal analysis, writing-original draft; T. D.: methodology, investigation; R. V.: funding acquisition, resources, supervision, writing-review and editing.

Conflicts of interest

The authors declare no conflict of interest.

Acknowledgements

The authors acknowledge the Centre for Research and Development of Scientific Instruments (CRDSI) and AIOT Lab at IIT Jodhpur, DRDO Jodhpur (Sujalam Building), IIT Jammu and Gitam University, Vishakhapatnam for access to the FACS, FE-SEM, FT-IR, XPS and XRD facilities, respectively. We are grateful to Prof. Surajit Ghosh for allowing us access to the fluorimeter in the DMD facility. R. V. acknowledges the funding support provided by the Department of Biotechnology (DBT), Government of India, for the Ramalingaswami Biomedical Fellowship (BT/RLF/Re-entry/17/2018), SEED grant (I/SEED/RRV/20200076) funded by IIT Jodhpur and Core Research Grant funded by SERB (CRG/2023/001189). Research Fellowship through PMRF (2202241) to Sarmistha Mazumder is duly acknowledged.

References

1 K. Kusada and H. Kitagawa, *Adv. Mater.*, 2016, **28**, 1129–1142.

2 O. Długosz, K. Szostak, A. Staroń, J. Pulit-Prociak and M. Banach, *Materials*, 2020, **13**(2), 279.

3 A. Tabassum, S. Ata, Y. Ding, I. U. Mohsin, S. A. K. Leghari, A. A. Al Kahtani, A. Nafady and M. Sohail, *ChemistrySelect*, 2024, **9**, e202403451.

4 S. Sajjad, B. Uzair, A. Shaukat, M. Jamshed, S. A. K. Leghari, M. Ismail and Q. Mansoor, *IET Nanobiotechnol.*, 2019, **13**, 435–440.

5 S. Abdolmaleki, A. Aliabadi and S. Khaksar, *J. Cancer Res. Clin. Oncol.*, 2024, **150**(4), 213.

6 S. B. Mali, *J. Maxillofac. Oral Surg.*, 2024, DOI: 10.1007/s12663-024-02374-3.

7 S. Naz, A. Gul, M. Zia and R. Javed, *Appl. Microbiol. Biotechnol.*, 2023, **107**, 1039–1061.

8 Q. Xiong, A. Liu, Q. Ren, Y. Xue, X. Yu, Y. Ying, H. Gao, H. Tan, Z. Zhang, W. Li, S. Zeng and C. Xu, *Cell Death Dis.*, 2020, **11**, 366.

9 M. L. Kung, S. L. Hsieh, C. C. Wu, T. H. Chu, Y. C. Lin, B. W. Yeh and S. Hsieh, *Nanoscale*, 2015, **7**, 1820–1829.

10 S. Sicwetsha, S. Mvango, T. Nyokong and P. Mashazi, *J. Nanopart. Res.*, 2021, **23**, 227.

11 C. Angelé-Martínez, K. V. T. Nguyen, F. S. Ameer, J. N. Anker and J. L. Brumaghim, *Nanotoxicology*, 2017, **11**, 278–288.

12 Z. Yang, X. Hao, S. Chen, Z. Ma, W. Wang, C. Wang, L. Yue, H. Sun, Q. Shao, V. Murugadoss and Z. Guo, *J. Colloid Interface Sci.*, 2019, **533**, 13–23.

13 M. J. Woźniak-Budych, Ł. Przysiecka, B. M. Maciejewska, D. Wieczorek, K. Staszak, M. Jarek, T. Jesionowski and S. Jurga, *ACS Biomater. Sci. Eng.*, 2017, **3**, 3183–3194.

14 L. Xiong, H. Yu, C. Nie, Y. Xiao, Q. Zeng, G. Wang, B. Wang, H. Lv, Q. Li and S. Chen, *RSC Adv.*, 2017, **7**, 51822–51830.

15 H. Naatz, S. Lin, R. Li, W. Jiang, Z. Ji, C. H. Chang, J. Köser, J. Thöming, T. Xia, A. E. Nel, L. Mädler and S. Pokhrel, *ACS Nano*, 2017, **11**, 501–515.

16 A. Joshi, H. Naatz, K. Faber, S. Pokhrel and R. Dringen, *Neurochem. Res.*, 2020, **45**, 809–824.

17 L. Wu, F. Yang, Y. Xue, R. Gu, H. Liu, D. Xia and Y. Liu, *Mater. Today Bio*, 2023, **24**(19), 100595.

18 K. Nuthalapati, R. Vankayala, M. Shanmugam, S. Thangudu, C. S. Chiang and K. C. Hwang, *Small Sci.*, 2024, **4**(10), 2400191.

19 L. Lin, X. Song, Y. Chen, M. Rong, Y. Wang, L. Zhao, T. Zhao and X. Chen, *Anal. Chim. Acta*, 2015, **891**, 261–268.

20 X. Zhuang, X. Gao, C. Tian, D. Cui, F. Luan, Z. Wang, Y. Xiong and L. Chen, *Chem. Commun.*, 2020, **56**, 5755–5758.

21 M. M. Foroughi, S. Jahani, Z. Aramesh-Boroujeni, M. Rostaminasab Dolatabad and K. Shahbazkhani, *Ceram. Int.*, 2021, **47**, 19727–19736.

22 N. H. Ferreira, R. A. Furtado, A. B. Ribeiro, P. F. de Oliveira, S. D. Ozelin, L. D. R. de Souza, F. R. Neto, B. A. Miura, G. M. Magalhães, E. J. Nassar and D. C. Tavares, *J. Inorg. Biochem.*, 2018, **182**, 9–17.

23 J. A. M. Cosico, P. K. Ruales and M. C. Marquez, *Mater. Sci. Eng.*, 2017, **205**(1), 012027.

24 D. Kim, S. C. Kim, J. S. Bae, S. Kim, S. J. Kim and J. C. Park, *Inorg. Chem.*, 2016, **55**, 8359–8370.

25 H. Idriss, *Surf. Sci.*, 2021, **712**, 121894.

26 K. Wang, X. Dong, C. Zhao, X. Qian and Y. Xu, *Electrochim. Acta*, 2015, **152**, 433–442.

27 S. Singh and D. Singh, *J. Mater. Sci.: Mater. Electron.*, 2020, **31**, 5165–5175.

28 K. Binnemans, *Coord. Chem. Rev.*, 2015, **295**, 1–45.

29 R. Bunea, A. K. Saikumar and K. Sundaram, *Mater. Sci. Appl.*, 2021, **12**, 182–196.

30 G. Murugadoss, S. Salla, M. R. Kumar, N. Kandhasamy, H. Al Garalleh, M. Garaleh, K. Brindhadevi and A. Pugazhendhi, *Environ. Res.*, 2023, **220**, 115171.

31 T. Kakkar, N. Thomas, E. Kumi-Barimah, G. Jose and S. Saha, *J. Biophotonics*, 2017, **11**(5), 1–10.

32 K. Szyszka, S. Targońska, A. Lewińska, A. Watras and R. J. Wiglusz, *Nanomaterials*, 2021, **11**, 464.

33 J. A. Jiménez, *Spectrochim. Acta, Part A*, 2015, **145**, 482–486.

34 J. A. Jiménez, *Spectrochim. Acta, Part A*, 2017, **173**, 979–985.

35 X. Liu, B. Li, F. Fu, K. Xu, R. Zou, Q. Wang, B. Zhang, Z. Chen and J. Hu, *Dalton Trans.*, 2014, **43**, 11709–11715.

36 R. Abbasi, G. Shineh, M. Mobaraki, S. Doughty and L. Tayebi, *J. Nanopart. Res.*, 2023, **25**, 43.

37 Y. Wang, F. Yang, H. X. Zhang, X. Y. Zi, X. H. Pan, F. Chen, W. D. Luo, J. X. Li, H. Y. Zhu and Y. P. Hu, *Cell Death Dis.*, 2013, **4**, e783.

38 M. A. Siddiqui, H. A. Alhadlaq, J. Ahmad, A. A. Al-Khedhairy, J. Musarrat and M. Ahamed, *PLoS One*, 2013, **8**(8), e69534.

39 M. Shanmugam, N. Kuthala, R. Vankayala, C. S. Chiang, X. Kong and K. C. Hwang, *ACS Nano*, 2021, **15**, 14404–14418.

40 E. Moschini, G. Colombo, G. Chirico, G. Capitani, I. Dalle-Donne and P. Mantecca, *Sci. Rep.*, 2023, **13**, 2326.

41 L. C. Crowley, A. P. Scott, B. J. Marfell, J. A. Boughaba, G. Chojnowski and N. J. Waterhouse, *Cold Spring Harbor Protocols*, 2016, **2016**, 647–651.

42 I. J. Marques, P. D. Vaz, A. V. Girão, M. M. Nolasco and C. D. Nunes, *New J. Chem.*, 2023, **47**, 21924–21936.

43 A. Kessler, P. Huang, E. Blomberg and I. Odnevall, *Chem. Res. Toxicol.*, 2023, **36**, 1891–1900.

44 P. F. Wei, L. Zhang, S. K. Nethi, A. K. Barui, J. Lin, W. Zhou, Y. Shen, N. Man, Y. J. Zhang, J. Xu, C. R. Patra and L. P. Wen, *Biomaterials*, 2014, **35**, 899–907.

45 J. MacHhi, P. Yeapuri, M. Markovic, M. Patel, W. Yan, Y. Lu, J. D. Cohen, M. Hasan, M. M. Abdelmoaty, Y. Zhou, H. Xiong, X. Wang, R. L. Mosley, H. E. Gendelman and B. D. Kevadiya, *ACS Chem. Neurosci.*, 2022, **13**, 1232–1244.

46 B. Wiatrak, P. Sobierajska, M. Szandruk-Bender, P. Jawien, M. Janeczek, M. Dobrzynski, P. Pistor, A. Szelag and R. J. Wiglusz, *Int. J. Mol. Sci.*, 2021, **22**(9), 4454.

47 Y. Hernández-Castillo, M. García-Hernández, A. López-Marure, J. H. Luna-Domínguez, P. Y. López-Camacho, Á. de and J. Morales-Ramírez, *Ceram. Int.*, 2019, **45**, 2303–2308.

48 E. Eruslanov and S. Kusmartsev, *Methods Mol. Biol.*, 2010, **594**, 57–72.

49 E. O. Gubernatorova, X. Liu, A. Othman, W. T. Muraoka, E. P. Koroleva, S. Andreescu and A. V. Tumanov, *Adv. Healthcare Mater.*, 2017, **6**(14), 1700176.

50 M. Shi, H. S. Kwon, Z. Peng, A. Elder and H. Yang, *ACS Nano*, 2012, **6**, 2157–2164.

51 H. Wiseman and B. Halliwell, *Biochem. J.*, 1996, **313**, 17–29.